JMES The International Journal of
Mechanical Engineering and Sciences
https://journal.its.ac.id/index.php/jmes/index
e-ISSN 2580-7471

Unified 1D Dynamic Modelling of Three Heat Exchanger Types with Numerical Verification and PI Control

Rohid Kusuma Wardana*, Mohamad Yamin

Department of Mechanical Engineering, Universitas Gunadarma, Indonesia

Received: 7 August 2026, Revised: 10 October 2026, Accepted: 27 October 2026

Abstract

This study develops a unified 1D dynamic thermal simulator for double-pipe, shell & tube, and plate heat exchangers using one three-domain partial differential equation (PDE) structure (hot fluid, wall, cold fluid), one adaptive Nusselt engine with smooth regime blending, and one feedforward-feedback control architecture. Spatial discretization is verified with the Grid Convergence Index (GCI; observed order 0.99–1.00, fine-grid GCI 0.04–0.30%). Steady-state heat duty agrees with analytical effectiveness-number of transfer units (NTU) solutions to within 0.7%; the 1D counter-flow shell & tube model transfers 7.6% more heat than the actual one-shell-pass, two-tube-pass configuration. The lumped-wall assumption holds for the plate exchanger (Biot number Bi ≈ 0.03) but not for double-pipe and shell & tube exchangers (Bi ≈ 1.29 and 0.62), limiting transient wall fidelity. For a 10 °C hot inlet step, proportional-integral (PI) control tuned by Simple Internal Model Control (SIMC) rules, with and without feedforward, returns outlet temperature to within ± 0.5 °C in 3.5–38 s. Feedforward shortens recovery time three- to six-fold in the two cases where the process time constant exceeds the transport delay ($\tau/\theta > 3$), but gives no benefit in the delay-dominated plate case. Transient predictions lack experimental validation.

Keywords: Dynamic simulation, grid convergence index, heat exchanger, partial differential equation, SIMC tuning

1. Introduction

Heat exchangers (HE) are crucial in many process industries, where outlet temperature stability affects energy use and process integrity [1]; flow fluctuations, pump degradation, and variations in the heating medium cause setpoint deviations that risk product quality [2]. HE design has matured, with established correlations for laminar flow [3], transitional and turbulent flow [4], shell-side cross-flow [5], and chevron plates [6]. Simulation tools built on them still show three limitations: most treat a single HE type at steady state, so cross-type comparisons rarely share a common basis; discretization errors are rarely verified; and frameworks coupling transient behaviour with closed-loop control remain uncommon.

Recent studies address these limitations only in part. Zhao et al. [7] simulate exchanger dynamics in the frequency domain, which does not directly yield the time-domain trajectory needed for nonlinear controller testing; Granda et al. [8] approximate transients from a steady-state model for low-heat-capacity media; Yang et al. [9] work at the network level, without the internal profile of a single unit; and Mechhoud and Belkhatir [10] develop adaptive bilinear control for one parallel-flow geometry. Machine learning and physics-informed neural network (PINN) surrogates [11–13] and digital twins for fouling diagnosis [14–16] depend on white-box simulators for training data and validation, and physics-based simulation is likewise used in boiler erosion [17], wind turbine aerodynamics [18], and plant thermal distribution [19]. Table 1 positions the present framework.

The contribution of this study is the integration, within one cross-geometric framework, of (i) a 1D three-domain PDE model with axial wall conduction, (ii) an adaptive Nusselt engine with smooth regime blending, (iii) formal spatial verification by Richardson extrapolation [20] and the Grid Convergence Index (GCI) [21], and (iv) a feedforward (FF) plus proportional-integral (PI) control layer tuned with the Simple Internal Model Control (SIMC) rules [22], with the feedforward contribution isolated through a PI-only comparison. The shell & tube exchanger is represented as an equivalent 1D counter-flow model, not a geometric replica of a multi-pass unit.

2. Numerical Methodology

The framework is implemented in MATLAB R2024b. Unified refers to a single 1D three-domain PDE structure, Nusselt engine, and control architecture shared by the three geometries, which differ only through flow areas, perimeters, hydraulic diameters, wall resistances, and side-specific correlations. For the shell & tube case this is an

*Corresponding author. Email: rohidkusumawardana@gmail.com, phone: +62 8881326331
© 2026. The Authors. Published by DRPM ITS

Table 1. Positioning of the present framework relative to previous studies.

Study	Geometries	Approach	Spatial transient profile	Grid verification	Closed-loop control
Zhao et al. [7]	Generic	Frequency domain	Indirect	No	No
Granda et al. [8]	Low-heat-capacity media	Steady-state-based transient	Approximate	No	No
Yang et al. [9]	Networks	Analytical, network level	No	No	No
Mechhoud and Belkhatir [10]	Parallel-flow	Bilinear PDE	Yes	No	Adaptive bilinear
ML and PINN surrogates [11–13]	Various	Data-driven	Training-data dependent	Not applicable	Typically no
Present	Double-pipe, shell & tube (equivalent 1D), plate	1D three-domain PDE, axial wall conduction	Yes	Richardson and GCI	FF plus SIMC PI, PI-only comparison

Table 2. Simulation parameters for reproducibility.

Category	Parameter	Value
Geometry (double-pipe)	$D_{ti}; D_{to}; D_{si}; L$	0.02664 m; 0.0334 m; 0.0525 m; 4 × 4.877 m = 19.508 m
Geometry (shell & tube)	$D_{ti}; D_{to}; D_{si}; N_t; P_t$ (triangular); $B; L$	0.01482 m; 0.01905 m; 0.3378 m; 124; 0.02381 m; 0.1524 m; 4.877 m (one equivalent pass)
Geometry (plate)	$b; W; L; \beta; \phi; N_{\mathrm{ch}}$ (per side); t_w	0.00254 m; 0.110 m; 0.380 m; $60°$; 1.17; 10; 0.0005 m
Wall material (all cases)	$k_w; \rho_w; c_{p,w}$	50 W/(m K); 7850 kg/m^3; 490 J/(kg K)
Hydraulic diameter D_h	Tube side; annulus; shell side; plate channel	D_{ti}; $D_{si} - D_{to}$; D_e of Equation 19 (0.01376 m); $2b/\phi$ (0.00434 m)
Duty at nominal flows	$C_h; C_c; \Delta P_h; \Delta P_c$	Double-pipe: 10,567 W/K; 15,799 W/K; 109.6 kPa; 83.0 kPa Shell & tube: 264,651 W/K; 105,422 W/K; 25.1 kPa; 513.6 kPa Plate: 348 W/K; 418 W/K; 0.112 kPa; 0.168 kPa
Actuator limits	$\dot{m}_{c,\min}; \dot{m}_{c,\max}$	0.01 kg/s; 3.8 kg/s (double-pipe), 75.9 kg/s (shell & tube), 1.0 kg/s (plate)
Numerical settings	Grid criterion; CFL factor; t_{gi}; tolerance; t_{end}; t_{dist}; controller activation	$\lvert\Delta T_{h,\mathrm{out}}\rvert < 0.1$ °C; 0.7; 100 s; ± 0.5 °C; 600 s; 300 s; 20 s

equivalent 1D counter-current representation with all tubes in one parallel pass, not a model of the baffled multi-pass flow path.

2.1. System Parameters and Operating Conditions

Geometry and numerical settings are listed in Table 2 [3, 23]. Both streams are liquid water; properties are interpolated at every time step from saturated-liquid tables (0.01 °C to 360 °C) at each stream's axial-average temperature. The double-pipe consists of four 4.877 m (16 ft) legs in series (image = 19.5 m). In the shell & tube bundle the hot fluid is distributed over all 124 tubes in parallel. The plate exchanger has ten channels per side and 0.5 mm plates.

Each setpoint lies within the range attainable with the cold-side actuator: 60 °C for the double-pipe and plate exchangers (3.19 kg/s and 0.044 kg/s). For the shell & tube unit, 60 °C would require more than 110 kg/s, be-

Table 3. Operating scenarios for dynamic thermal control evaluation.

HE Type	$T_{h,\mathrm{in}}$ (°C)	$T_{c,\mathrm{in}}$ (°C)	$\dot{m}_h$ (kg/s)	$\dot{m}_c$ (kg/s)	Setpoint T_s (°C)	t_{dist} (s)	Disturbance Scenario
Double-Pipe	93.3	26.7	2.52	3.78	60	300	Step of $T_{h,\mathrm{in}}$ to 83.3 °C
Shell & Tube	93.3	26.7	63	25.2	65	300	Step of $T_{h,\mathrm{in}}$ to 83.3 °C
Plate	93.3	26.7	0.083	0.1	60	300	Step of $T_{h,\mathrm{in}}$ to 83.3 °C

Table 4. Hierarchy and ranges of the adaptive Nusselt correlations.

Correlation	Flow Geometry	Re Condition	Pr Condition	Ref.
Sieder-Tate, bounded by 3.66	Tube side, annulus	$Re < 2300$	0.48 to 16,700	[24]
Gnielinski	Tube side, annulus	$2300 \le Re \le 5 \times 10^6$	0.5 to 2000	[4]
Lyon	Internal (not exercised)	$Re > 10^4$	$Pr < 0.1$	[23]
Petukhov	Internal (not exercised)	$10^4 < Re < 5 \times 10^6$	$Pr > 120$	[24]
Dittus-Boelter	Internal (not exercised)	$Re > 10^4$	$0.1 \le Pr < 0.5$	[24]
Kern	Shell side	2×10^3 to 10^6	–	[5]
Martin (generalized Lévêque)	Plate channels	approx. 200 to 10^4	–	[6, 25]

yond the 75.9 kg/s actuator capacity (62.6 °C is the lowest attainable), so its setpoint is 65 °C (57.7 kg/s).

The duty row of Table 2 reports C_h, C_c, and ΔP, which differ by a factor of about 760 (C_h) and by more than three orders of magnitude (ΔP); the shell-side pressure drop, Equation (23), is high because the nominal cross-flow mass velocity (2.4×10^3 kg/(m^2 s)) is at the upper end of practice and the Kern method is approximate. The dynamic scenarios are listed in Table 3.

2.2. Dynamic Partial Differential Equation (PDE) Modelling

The two fluids are described by 1D hyperbolic PDEs [7–9] coupled to a parabolic wall energy balance; for the hot fluid, the wall, and the counter-current cold fluid:

$$\frac{\partial T_h}{\partial t} = -u_h \frac{\partial T_h}{\partial x} - \frac{q_{h,w}}{\rho_h c_{p,h} A_h} \tag{1}$$

$$\frac{\partial T_w}{\partial t} = \frac{q_{h,w} - q_{w,c}}{\rho_w c_{p,w} A_w} + \alpha_w \frac{\partial^2 T_w}{\partial x^2} \tag{2}$$

$$\frac{\partial T_c}{\partial t} = u_c \frac{\partial T_c}{\partial x} + \frac{q_{w,c}}{\rho_c c_{p,c} A_c} \tag{3}$$

The transverse heat flows per unit length use the local convective coefficients with one half of the wall conduction resistance on each side of the lumped wall node:

$$q_{h,w} = \frac{T_h - T_w}{\dfrac{1}{h_h P_h} + \dfrac{R_w}{2}}, \qquad q_{w,c} = \frac{T_w - T_c}{\dfrac{R_w}{2} + \dfrac{1}{h_c P_c}} \tag{4}$$

$$R_w = \frac{\ln(D_{to}/D_{ti})}{2\pi k_w N_t} \quad \text{(tubes, } N_t = 1 \text{ for the double-pipe)} \qquad R_w = \frac{t_w}{k_w W N_{ch}} \quad \text{(plates)} \tag{5}$$

The steady-state overall resistance thus includes the wall conduction, so the lumped wall affects only the transient response. The axial term uses $\alpha_w = k_w/(\rho_w c_{p,w})$ with adiabatic wall ends.

The hot fluid enters at $x = 0$ with $u_h = \dot{m}_h/(\rho_h A_h)$ and the cold fluid at $x = L$ with speed $u_c = \dot{m}_c/(\rho_c A_c)$ in the negative direction, hence the positive advection term of Equation (3). Boundary conditions are $T_h(0,t) = T_{h,\mathrm{in}}(t)$ and $T_c(L,t) = T_{c,\mathrm{in}}(t)$; the initial conditions follow an exponential profile that accelerates convergence:

Table 5. Spatial grid independence study ($T_{h,\mathrm{out}}$) after $t_{\mathrm{gi}} = 100$ s; CPU time per 100 s of simulated time.

N	Double Pipe			Shell & Tube			Plate		
	$T_{h,\mathrm{out}}$ (°C)	Δ (°C)	CPU (s)	$T_{h,\mathrm{out}}$ (°C)	Δ (°C)	CPU (s)	$T_{h,\mathrm{out}}$ (°C)	Δ (°C)	CPU (s)
30	58.43	–	0.37	73.84	–	0.55	41.08	–	0.07
50	58.23	0.20	0.57	73.72	0.12	0.96	40.59	0.49	0.11
75	58.13	0.10	0.71	73.66	0.06	1.44	40.35	0.25	0.17
100	58.08	0.05	0.99	73.63	0.03	1.87	40.22	0.13	0.24
150	58.03	0.05	1.77	73.60	0.03	3.07	40.10	0.13	0.38
200	58.00	0.03	2.25	73.58	0.02	4.24	40.03	0.06	0.52
300	57.98	0.03	3.53	73.57	0.02	6.60	39.97	0.06	0.85
400	57.97	0.01	5.18	73.56	0.01	9.41	39.94	0.03	1.25
500	57.96	0.01	7.12	73.55	0.01	13.10	39.92	0.02	1.68

Table 6. GCI convergence parameters and asymptotic-range check.

HE Type	Order (p)	GCI_{fine} at $N_1 = 400$	Asymptotic Ratio	f_{ext} (°C)	Error estimate at N_{opt}
Double-Pipe	0.995	0.082%	0.999	57.929	0.33% ($N_{\mathrm{opt}} = 100$)
Shell & Tube	0.995	0.040%	1.000	73.536	0.21% ($N_{\mathrm{opt}} = 75$)
Plate	0.993	0.298%	0.998	39.844	0.59% ($N_{\mathrm{opt}} = 200$)

$$c_v(x) = \frac{1 - e^{-3x/L}}{1 - e^{-3}} \tag{6}$$

$$T_h(x,0) = T_{h,in} - (T_{h,in} - T_{sp})\, c_v(x) \tag{7}$$

$$T_c(x,0) = (T_{h,in} - 10) - [(T_{h,in} - 10) - T_{c,in}]\, c_v(x) \tag{8}$$

$$T_w(x,0) = 0.5\,[T_h(x,0) + T_c(x,0)] \tag{9}$$

The 10 °C in Equation (8) affects only the initial transient.

2.3. Adaptive Nusselt Correlation Engine

Convective coefficients are evaluated at every node and time step from Re and Pr based on the stream-average properties and the hydraulic diameter of each passage. The smooth-tube Darcy friction factor follows Petukhov [24]:

$$f = (0.79 \ln Re - 1.64)^{-2} \tag{10}$$

For internal flow, the laminar branch uses the Sieder-Tate correlation bounded by the fully developed asymptote [24], and the transitional and turbulent branches use the Gnielinski correlation [4] (Table 4):

$$Nu_{lam} = \max\left[3.66,\ 1.86\left(Re \cdot Pr \cdot \frac{D_h}{L}\right)^{1/3}\left(\frac{\mu}{\mu_w}\right)^{0.14}\right] \tag{11}$$

$$Nu_{Gn} = \frac{(f/8)(Re - 1000)Pr}{1 + 12.7(f/8)^{0.5}\left(Pr^{2/3} - 1\right)} \tag{12}$$

For generality, the turbulent branch ($Re > 10^4$) also includes the Lyon correlation for liquid metals ($Pr < 0.1$) [23], Petukhov [24], and Dittus-Boelter [24] as a fallback outside the Prandtl range of Gnielinski:

$$Nu_{Lyon} = 7.0 + 0.025\,(Re \cdot Pr)^{0.8} \tag{13}$$

$$Nu_{Pet} = \frac{(f/8)\, Re \cdot Pr}{1.07 + 12.7(f/8)^{0.5}\left(Pr^{2/3} - 1\right)}\left(\frac{\mu}{\mu_w}\right)^{0.14} \tag{14}$$

$$Nu_{DB} = 0.023\, Re^{0.8} Pr^{n}$$
$$n = 0.4 \text{ (fluid heated)}, \quad n = 0.3 \text{ (fluid cooled)} \tag{15}$$

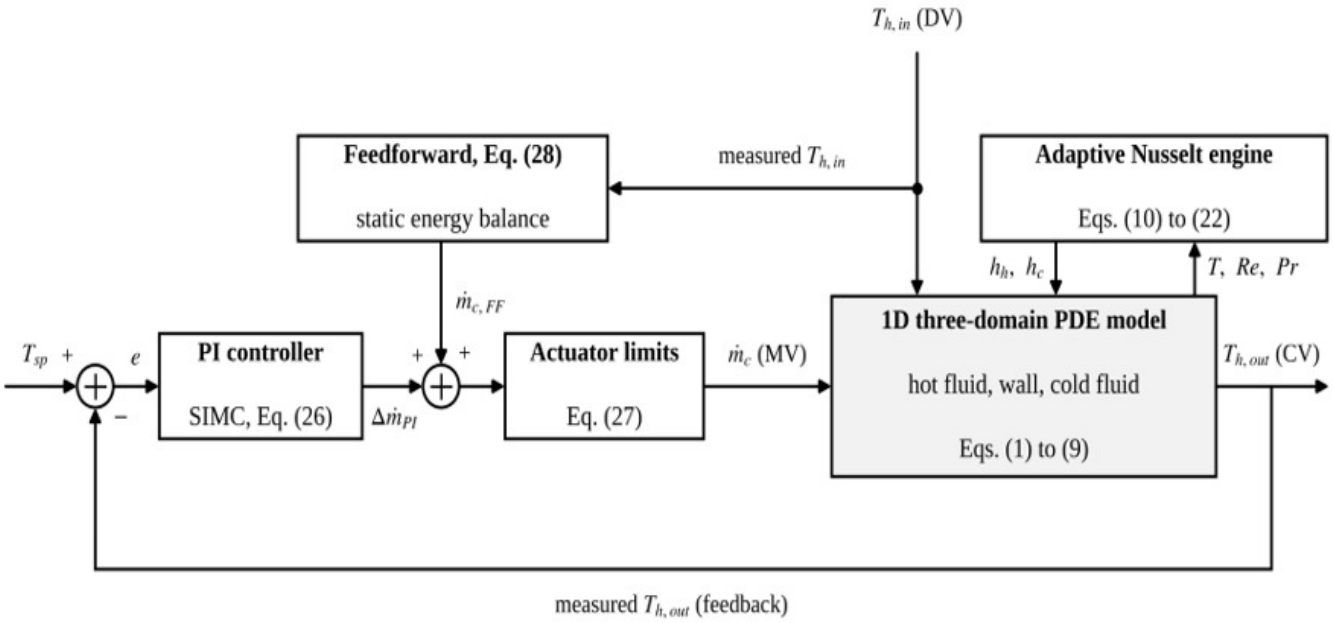


Figure 1. Block diagram of the integrated dynamic simulator: DV, disturbance variable; MV, manipulated variable; CV, controlled variable.

Table 7. Correlation engine benchmark (Level 1).

Flow geometry	Engine correlation	Benchmark	Conditions	Deviation	Remark
Tube side	Gnielinski (engine)	Gnielinski, independent [4]	$Re = 1.1 \times 10^5$ to 3.2×10^5, $Pr = 2.1$ to 2.6	$< 10^{-6}$	Implementation check
Tube side	Gnielinski (engine)	Dittus-Boelter [24]	Same points, $n = 0.3$ and 0.4	9% to 22% lower	Within $\pm 25\%$ uncertainty
Plate	Martin	Muley and Manglik [27]	$Re = 1000$ to 2000, $Pr = 2.5$, $\beta = 60°$, $\phi = 1.29$	Martin 5% to 9% higher	Above operating Re

For water ($2 < Pr < 5$) the turbulent branch always resolves to Gnielinski, so Equations (13) to (15) are not exercised. Instead of switching discretely at the regime thresholds, the engine blends the branches with hyperbolic-tangent weights centred at $Re = 2300$ and 10^4:

$$Nu = (1 - w_1)\, Nu_{lam} + w_1 \left[(1 - w_2)\, Nu_{Gn} + w_2\, Nu_{turb}\right] \tag{16}$$

$$\begin{aligned} w_1 &= \frac{1}{2}\left[1 + \tanh\left(\frac{Re - 2300}{200}\right)\right] \\ w_2 &= \frac{1}{2}\left[1 + \tanh\left(\frac{Re - 10^4}{1000}\right)\right] \end{aligned} \tag{17}$$

where Nu_{turb} is the branch selected by the Prandtl number; the widths 200 and 1000 confine the blending to narrow bands while keeping h continuous.

The shell side uses the Kern correlation [5] with the triangular-layout equivalent diameter and the cross-flow area $D_{si}(P_t - D_{to})B/P_t$:

$$Nu = 0.36\, Re^{0.55} Pr^{1/3} \left(\frac{\mu}{\mu_w}\right)^{0.14} \tag{18}$$

$$D_e = \frac{4\left(\frac{\sqrt{3}}{4} P_t^2 - \frac{\pi}{8} D_{to}^2\right)}{\pi D_{to}/2} \tag{19}$$

Both plate sides use the generalized Lévêque correlation of Martin [6] in the VDI Heat Atlas form [25], which ties Nu to the Darcy-type friction factor f_d of the corrugated channel and the chevron angle β:

$$Nu = 0.122\, Pr^{1/3} \left(\frac{\mu}{\mu_w}\right)^{1/6} \left[f_d\, Re^2 \sin(2\beta)\right]^{0.374} \tag{20}$$

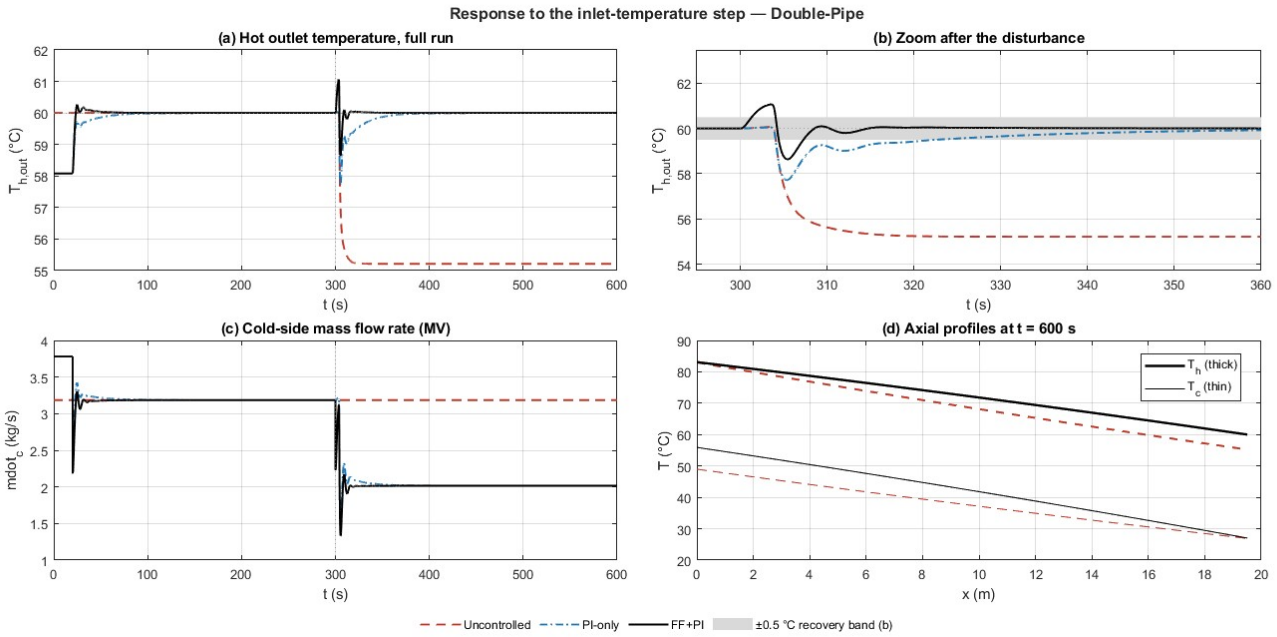


Figure 2. Double-pipe response to the 10 °C step decrease in $T_{h,\mathrm{in}}$ at $t = 300$ s: (a) hot outlet temperature; (b) zoom after the disturbance with the ± 0.5 °C recovery band; (c) cold-side mass flow rate; (d) axial temperature profiles at $t = 600$ s.

Table 8. Effectiveness-NTU analytical comparison summary (Level 2).

HE Type	Comparison	NTU	ε	$T_{h,\mathrm{out}}$ sim vs. reference (°C)	Duty Deviation	Status
Double-Pipe	Counter-flow, U from correlations	0.962	0.531	58.08 / 57.93	0.44%	Agrees with analytical solution
Shell & Tube	Counter-flow, U from correlations	1.686	0.745	73.66 / 73.54	0.63%	Agrees with analytical solution
Shell & Tube	1-2 pass at the NTU, C_r of the simulated duty	1.660	0.688	73.66 / 75.05	7.6%	Multi-pass effect, $F_t = 0.845$
Plate	Counter-flow, U from correlations	3.099	0.803	40.03 / 39.84	0.37%	Agrees with analytical solution

$$\frac{1}{\sqrt{f_d}} = \frac{\cos\beta}{\sqrt{0.18\tan\beta + 0.36\sin\beta + f_{d0}/\cos\beta}} + \frac{1-\cos\beta}{\sqrt{3.8 f_{d1}}} \tag{21}$$

$$f_{d0} = \begin{cases} 64/Re, & Re < 2000 \\ \left(1.8\log_{10} Re - 1.5\right)^{-2}, & Re \geq 2000 \end{cases}$$
$$f_{d1} = \begin{cases} 597/Re + 3.85, & Re < 2000 \\ 39\, Re^{-0.289}, & Re \geq 2000 \end{cases} \tag{22}$$

with $D_h = 2b/\phi$ and Re based on the channel velocity; the correlation was fitted to data spanning approximately $200 < Re < 10^4$ [6, 25]. Pressure drops are accumulated over the nodes with the friction factor of each passage (Equation (10) or $64/Re$ for tube and annulus, the Kern shell-side factor [5], and f_d for the plate channels):

$$\Delta P = \sum_{i=1}^{N} f_i \frac{\Delta x}{D_h} \frac{\rho_i u_i^2}{2} \tag{23}$$

2.4. Numerical Discretization and CFL Stability

The domain is discretized into N nodes; advection uses a first-order explicit upwind scheme [26], axial conduction a central difference, and time integration the explicit Euler method. The time step satisfies the fluid Courant-Friedrichs-Lewy (CFL) condition with a safety factor of 0.7 and the Fourier limit of the wall conduction term:

$$\Delta t = \min\left[0.7\frac{\Delta x}{\max(u_h, u_c)},\ 0.5\frac{\Delta x^2}{\alpha_w}\right] \tag{24}$$

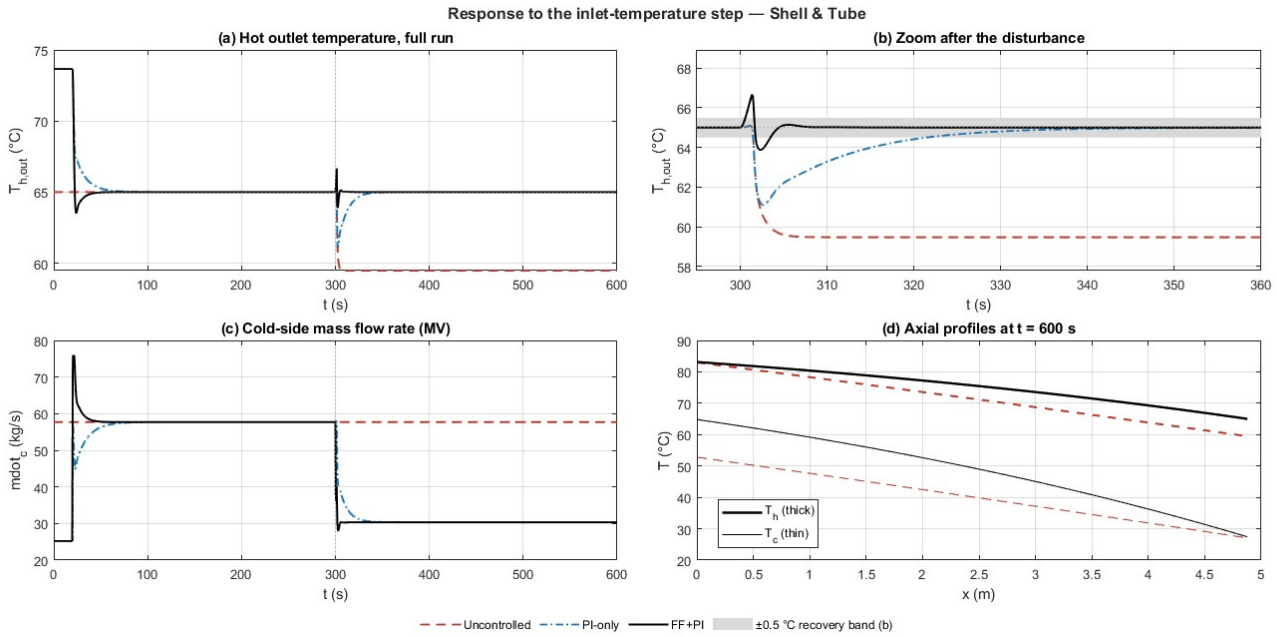


Figure 3. Shell & tube response to the 10 °C step decrease in $T_{h,\mathrm{in}}$ at $t = 300$ s: (a) hot outlet temperature; (b) zoom after the disturbance with the ± 0.5 °C recovery band; (c) cold-side mass flow rate; (d) axial temperature profiles at $t = 600$ s.

Table 9. Biot number assessment of the lumped wall.

HE Type	h_{avg} (W/m^{2}K)	L_{char} (m)	Bi	Lumped-capacitance valid?
Double-Pipe	19,118	0.00338	1.29	No ($Bi \geq 0.1$)
Shell & Tube	14,690	0.00212	0.62	No ($Bi \geq 0.1$)
Plate	2,632	0.00050	0.026	Yes

2.5. Control System Synthesis

The manipulated variable is the cold flow, the controlled variable the hot outlet temperature, and the disturbance the hot inlet temperature (Figure 1). The process is approximated as first order plus dead time (FOPDT): K_p is identified at the nominal flows of Table 3 from the steady-state change of $T_{h,out}$ for a step in $\dot{m}_c$ of 5% of the nominal value (at least 0.05 kg/s, which is 50% for the plate), θ is the hot-side transport time, and τ the ratio of thermal capacitance to the overall conductance at the nominal point:

$$\theta = \frac{L}{u_h}, \qquad \tau = \frac{C_{sys}}{UA_{eff}}$$
$$C_{sys} = (\rho_h c_{p,h} A_h + \rho_w c_{p,w} A_w + \rho_c c_{p,c} A_c)\, L \tag{25}$$
$$UA_{eff} = L \left[\frac{1}{h_h P_h} + R_w + \frac{1}{h_c P_c} \right]^{-1}$$

The PI gains follow the SIMC rules [22] with $\tau_c = \theta$:

$$K_c = \frac{\tau}{|K_p|(\tau_c + \theta)}, \qquad \tau_I = \min\left[\tau,\ 4(\tau_c + \theta)\right] \tag{26}$$

The control law adds a static energy-balance feedforward term to the PI correction and is bounded by the actuator limits:

$$\dot{m}_c(t) = \mathrm{sat}\left[\dot{m}_{c,FF}(t) + K_c\, e(t) + \frac{K_c}{\tau_I} \int_0^t e\, dt' \right] \tag{27}$$
$$e = T_{h,out} - T_{sp}, \qquad \dot{m}_{c,min} \leq \dot{m}_c \leq \dot{m}_{c,max}$$

$$\dot{m}_{c,FF} = \frac{\dot{m}_h\, c_{p,h}\, (T_{h,in} - T_{sp})}{c_{p,c} \max\left(T_{c,out} - T_{c,in},\ 5\,^\circ\mathrm{C}\right)} \tag{28}$$

Equation (28) gives the cold flow that would remove the heat required to bring the measured inlet temperature to the setpoint at the current cold-side temperature rise; in the PI-only configuration it is replaced by the nominal cold flow. The integral term is clamped (anti-windup), and the controller is activated at $t = 20$ s. The uncontrolled configuration holds $\dot{m}_c$ at the value that gives $T_{h,out} = T_{sp}$ before the disturbance. Performance is quantified by the integral of squared error (ISE) after the disturbance and by the recovery time t_r, after which $T_{h,out}$ stays within ± 0.5 °C of the setpoint:

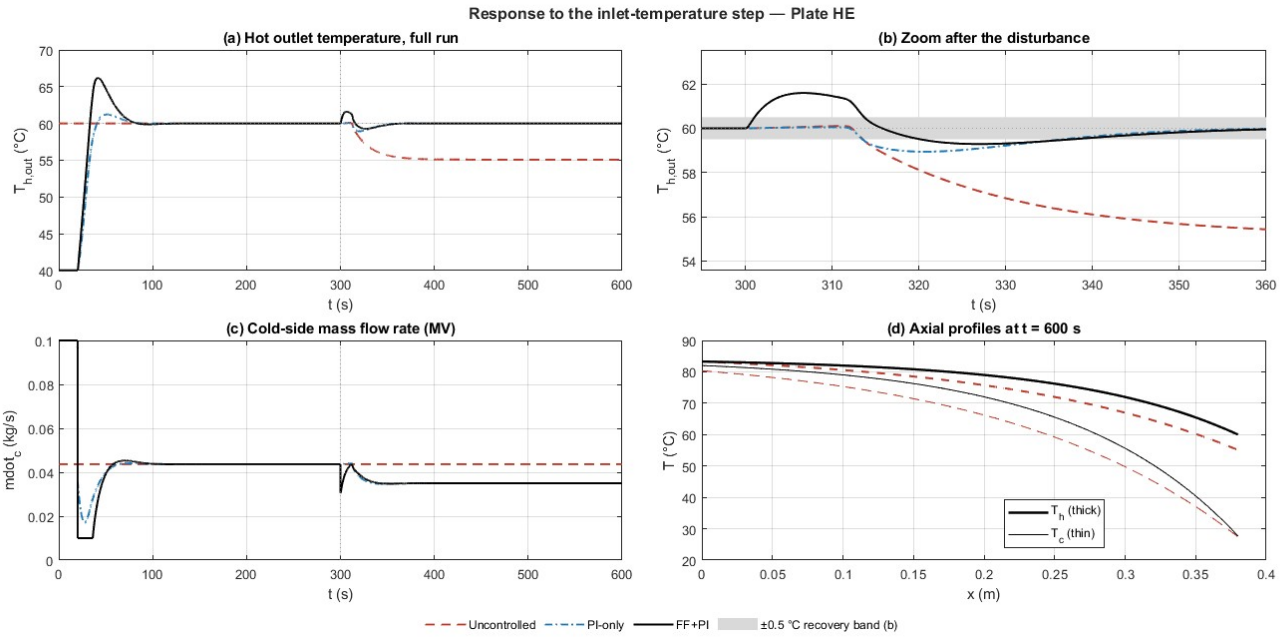


Figure 4. Plate HE response to the 10 °C step decrease in $T_{h,\mathrm{in}}$ at $t = 300$ s: (a) hot outlet temperature; (b) zoom after the disturbance with the ± 0.5 °C recovery band; (c) cold-side mass flow rate; (d) axial temperature profiles at $t = 600$ s.

Table 10. Re, Pr, and Nu operating ranges over the transient simulations.

HE Type	Side	***Re* range**	***Pr* range**	***Nu* range**
Double Pipe	Hot (tube)	293,087 to 323,909	2.347 to 2.614	931.6 to 955.8
	Cold (annulus)	30,383 to 82,596	4.168 to 4.568	174.7 to 418.8
Shell & Tube	Hot (tube)	110,205 to 130,987	2.089 to 2.512	401.5 to 420.9
	Cold (shell)	65,845 to 183,844	3.221 to 4.335	241.2 to 429.4
Plate	Hot	295 to 386	2.095 to 2.798	17.0 to 18.2
	Cold	27 to 270	2.425 to 3.770	5.70 to 17.8

$$ISE = \int_{t_{dist}}^{t_{end}} \left[T_{h,out}(t) - T_{sp}\right]^2 dt \tag{29}$$

2.6. Verification and Analytical Comparison Procedure

Verification (Richardson extrapolation, GCI, pure-advection test) checks that the equations are solved correctly, the effectiveness-NTU comparison checks the steady state against closed-form theory, and no experimental validation was performed. The GCI uses three grids with refinement ratio $r = 2$ [20, 21]:

$$p = \frac{1}{\ln r} \ln \left| \frac{f_3 - f_2}{f_2 - f_1} \right| \tag{30}$$

$$GCI_{fine} = \frac{F_s \left| \dfrac{f_2 - f_1}{f_1} \right|}{r^p - 1} \times 100\% \tag{31}$$

where f_1, f_2, f_3 are the steady-state outlet temperatures on the fine, medium, and coarse grids and $F_s = 1.25$ [21]; the asymptotic range is confirmed when $GCI_{coarse}/(r^p GCI_{fine}) \approx 160$ 1.

Level 1 benchmarks the engine against independent published correlations [24, 27]. Level 2 compares the steady-state duty and outlet temperatures of the PDE-model with the analytical effectiveness-NTU solution of the counter-flow exchanger [24, 28], with U computed from the correlations at the stream-average temperatures(independently of the simulated duty), and reports the closure $|Q_h - Q_c|/Q_h$; for the shell & tube exchanger the one-shell-pass, two-tube-pass solution [24, 28, 29] at the same NTU and capacity ratio isolates the multi-pass effect. The lumped wall is assessed with the Biot number:

$$\begin{aligned} Bi &= \frac{h_{avg} L_{char}}{k_w}, \qquad h_{avg} = \frac{1}{2}\left(h_h + h_c\right) \\ L_{char} &= \frac{D_{to} - D_{ti}}{2} \text{ (tubes)}, \quad t_w \text{ (plates)} \end{aligned} \tag{32}$$

Finally, a pure-advection test ($h_h = h_c = 0$, step in $T_{h,\mathrm{in}}$) checks that the outlet reproduces the step delayed by L/u_h, the 10% to 90% rise time quantifying numerical

Table 11. Process parameters, SIMC gains, and dynamic performance of the uncontrolled, PI-only, and FF+PI configurations.

HE Type	θ (s)	τ (s)	K_p (°C/(kg/s))	K_c ((kg/s)/°C)	τ_I (s)	Metric	Un-Ctrl	PI	FF+PI
Double Pipe	4.2	16.66	-2.77	0.715	16.66	Peak deviation (°C)	4.79	2.29	1.36
						ISE (°C² s)	6,702	22.8	5.76
						t_r (s)	–	22.5	7.3
Shell & Tube	1.61	5.18	-0.435	3.7	5.18	Peak deviation (°C)	5.52	3.90	1.67
						ISE (°C² s)	9,072	77.8	3.07
						t_r (s)	–	21.4	3.5
Plate	12.46	8.71	-109	0.0032	8.71	Peak deviation (°C)	4.91	1.06	1.6
						ISE (°C² s)	6,309	18.9	32.5
						t_r (s)	–	36.5	37.6

diffusion, and a cold-flow ramp across both Re thresholds checks the continuity of the blended engine.

3. Results and Discussion

3.1. Numerical Verification and Asymptotic Grid Convergence

The steady-state $T_{h,\mathrm{out}}$ was evaluated for $N = 30$ to 500 nodes (Table 5), each run integrated for $t_{gi} = 100$ s (at least eight residence times). With the criterion $|\Delta T_{h,\mathrm{out}}| < 0.10$ °C between refinements, the working grids are $N_{\mathrm{opt}} = 100$, 75, and 200 for the double-pipe, shell & tube, and plate exchangers, and were used for all transient simulations. The GCI procedure of Celik et al. [21] was applied to the triplet $N = 100, 200, 400$ (Table 6), together with the error estimate of the working grid, $F_s|(f_{N_{\mathrm{opt}}} - f_{\mathrm{ext}})/f_{N_{\mathrm{opt}}}|$, from the Richardson-extrapolated f_{ext}.

The observed order ($p \approx 0.99$ to 1.00) matches the first order of the upwind scheme, and the asymptotic ratios (0.998 to 1.000) place $N = 400$ in the asymptotic range; the error estimates of the working grids (0.16 °C to 0.24 °C) are below the ± 0.5 °C recovery tolerance. CPU time grows faster than linearly with N because the CFL-limited time step shrinks with Δx; at the working grids the simulator runs 70 to 190 times faster than real time.

The pure-advection test confirms that the scheme reproduces the transport delay without bias: the 50% arrival time of the outlet step is 4.25 s, 1.62 s, and 12.55 s at the working grids, against $L/u_h = 4.24$ s, 1.62 s, and 12.58 s (evaluated at the setpoint temperature, whereas θ in Table 11 uses the mean of the inlet and setpoint temperatures). The 10% to 90% rise time of the outlet step is 0.59 s, 0.26 s, and 1.23 s at the working grids and 0.30 s, 0.11 s, and 0.88 s at $N = 400$, the ratio expected for first-order numerical diffusion, and small compared with the process time constants.

3.2. Correlation Benchmark and Analytical Comparison

At Level 1 (Table 7), the engine reproduces the Gnielinski correlation evaluated independently at the tube-side operating points of Table 10 to within round-off (at the Re of Table 7 the weights w_1 and w_2 equal unity), and the Dittus-Boelter values are 9% to 22% lower depending on the exponent n, within the $\pm 25\%$ uncertainty of that correlation [24]. The Martin correlation is 5% to 9% higher than the data of Muley and Manglik [27] at their plate geometry ($\beta = 60°$, $\phi = 1.29$, $Re = 1000$ to 2000, $Pr = 2.5$); since the plate scenario operates at $Re < 400$, this confirms consistency at a representative point rather than over the full operating envelope.

At Level 2 (Table 8), with U from the correlations, the simulated duty agrees with the analytical counter-flow solution to within 0.44% (double-pipe), 0.63% (shell & tube), and 0.37% (plate), and $T_{h,\mathrm{out}}$ to within 0.2 °C; the residuals arise from the temperature dependence of the stream-average properties and from the discretization error. The energy balance closes to better than 10^{-9}. For the shell & tube exchanger, at the NTU and capacity ratio of the simulated duty ($NTU = 1.66$, $C_r = 0.398$), the counter-flow effectiveness is 0.740 whereas the 1-2 pass effectiveness is 0.688 ($F_t = 0.845$ [29], the log mean temperature difference (LMTD) correction factor at equal effectiveness); the 1D counter-flow model therefore transfers 7.6% more heat ($T_{h,\mathrm{out}} = 73.66$ °C versus 75.05 °C) than a 1-2 pass unit with the same bundle.

The deviation from the 1-2 pass solution is thus the multi-pass correction, not a generic modelling error. The single-pass representation also halves the tube-side velocity relative to a two-pass bundle; a per-pass flow area is a refinement left for future work.

3.3. Wall Lumped-Capacitance Assessment (Biot Number)

Table 9 gives the Biot number at the nominal operating point; the radially uniform wall of Equation (2) is

justified when $Bi < 0.1$. The lumped wall is justified only for the plate exchanger. For the double-pipe and shell & tube cases ($Bi = 1.29$ and 0.62), the inner wall surface responds faster to the hot stream, and the outer surface more slowly, than the single wall node, so the thermal lag between the two streams is represented only approximately. This affects mainly the process time constant and hence the recovery times in Table 11 for these two geometries, with a sign and size not quantified here, whereas the steady-state balance is unaffected because the wall resistance is included in Equation (4). The comparison between PI-only and FF+PI is expected to be less affected, since both use the same wall model. A radially discretized wall model is left for future work.

3.4. Computational Reliability and Numerical Stability

Discrete switching between correlations at $Re = 2300$ and 10^4 produces step discontinuities in h that can destabilize the explicit integration: at $Re = 2300$ and $Pr = 4.3$, a switch from the laminar asymptote to Gnielinski changes Nu from 3.66 to 13.2 within one time step. The blended formulation was verified with a ramp test on the double-pipe geometry (cold flow from 0.01 kg/s to 3.78 kg/s over 200 s, Re_c from 3.4×10^2 to 8.3×10^4): the largest change of the cold-side coefficient between consecutive time steps is 6%, at $Re \approx 2300$ where the blend is steepest, and $T_{h,\mathrm{out}}$ changes by less than 0.02 °C per step. No numerical anomaly was observed in any simulation, and the fluid CFL limit remains binding in all geometries.

3.5. Reynolds, Prandtl, and Nusselt Number Operating Ranges

Table 10 lists the extremes of Re, Pr, and Nu over all nodes and time steps of the three configurations (0 to 600 s). The double-pipe and shell & tube flows remain fully turbulent on both sides ($Re > 3 \times 10^4$), so no regime crossing occurs and the Gnielinski and Kern correlations are used within their ranges. The plate exchanger operates at $Re < 400$, in the laminar branch of Equation (22). The cold-side minimum ($Re \approx 27$) occurs at the actuator lower limit during the initial setpoint acquisition (before $t = 60$ s) and lies below the data range of the correlation ($Re > 200$). After the disturbance the cold-side Re stays between 190 and 270, close to the lower bound of that range, whereas the hot side ($Re = 295$ to 386, Table 10) lies within it. The plate results, particularly the absolute values of $T_{h,\mathrm{out}}$, U, and recovery time, therefore carry a correlation uncertainty whose size was not determined. It acts through the convective coefficients on U and the process time constant, and hence on the required cold flow and the SIMC gains of the plate loop, whereas the feedforward term of Equation (28) does not contain the coefficients explicitly. The absolute values of U and the recovery time are expected to be the most affected; the double-pipe and shell & tube results are not affected.

3.6. Dynamic Control Performance

Table 11 lists the FOPDT parameters and SIMC gains; τ/θ is 3.96, 3.22, and 0.70 for the double-pipe, shell & tube, and plate exchangers, so the transport delay dominates only in the plate case. The uncontrolled cold flows are 3.19 kg/s, 57.7 kg/s, and 0.0437 kg/s. Responses are shown in Figure 2, Figure 3, and Figure 4; the peak deviation is the largest $|T_{h,\mathrm{out}} - T_{sp}|$ after t_{dist}. For the double-pipe and shell & tube exchangers, where the lumped wall is not justified (Table 9), the peak deviations and recovery times below carry additional uncertainty from the wall model.

Without control, the 10 °C inlet step displaces the outlet by 4.8 °C, 5.5 °C, and 4.9 °C (final values 55.2 °C, 59.5 °C, and 55.1 °C), roughly half the inlet step. Both controlled configurations return $T_{h,\mathrm{out}}$ to the setpoint without offset and reduce the ISE by two to three orders of magnitude (factors of 120 to 330 for PI-only and 190 to 2950 for FF+PI). The cold flow stays within the actuator limits during the disturbance rejection (panels (c) of Figure 2, Figure 3, and Figure 4); the limits are reached only during the initial setpoint acquisition, before $t = 60$ s.

The benefit of the static feedforward term depends on τ/θ. For the double-pipe and shell & tube exchangers, FF+PI reduces the peak deviation from 2.29 °C to 1.36 °C and from 3.90 °C to 1.67 °C, shortens the recovery time from 22.5 s to 7.3 s and from 21.4 s to 3.5 s, and lowers the ISE by factors of 4 and 25 relative to PI-only. Panels (b) of Figure 2 and Figure 3 show the mechanism: the feedforward term reduces the cold flow as soon as the inlet temperature drops, before the disturbance front reaches the outlet after the delay θ, producing an excursion of opposite sign (+1.1 °C and +1.7 °C) followed by an undershoot (1.36 °C for the double-pipe, and smaller than the +1.7 °C excursion for the shell & tube), whereas feedback acts only after the undershoot develops. For the plate exchanger the same early action is detrimental: the cold flow is reduced 12.5 s before the colder fluid reaches the outlet, the outlet first rises by 1.6 °C, the undershoot (0.71 °C) is smaller than the PI-only peak deviation (1.06 °C), but the recovery time (37.6 s) is no shorter than PI-only (36.5 s) and the ISE is 72% higher. Equation (28) has no dynamic compensation for the disturbance path; a lead-lag or delayed feedforward term matched to θ is a natural extension. In the cases studied, the energy-balance feedforward was worthwhile for $\tau/\theta = 3.2$ and 4.0 and not for $\tau/\theta = 0.7$; the threshold between these values was not determined.

Absolute ISE and recovery times are not comparable across geometries, because the capacity rates ($C_h = 348$ W/K to 265 kW/K) differ by a factor of about 760 and the pressure drops ($\Delta P = 0.1$ kPa to 514 kPa) by more than three orders of magnitude (Table 2). The ISE ratios, the delay-normalized recovery time ($t_r/\theta = 1.7$, 2.2, and 3.0 for FF+PI; 5.4, 13.3, and 2.9 for PI-only), and the within-geometry PI-only versus FF+PI comparison are therefore used; a comparison at matched duty and

pressure drop is left for future work.

4. Conclusions

A unified 1D PDE dynamic thermal simulator was developed for double-pipe, shell & tube, and plate heat exchangers. Grid convergence was confirmed with the Grid Convergence Index (observed order 0.99 to 1.00, fine-grid GCI 0.04% to 0.30%), and the pure-advection test showed that the transport delay is reproduced without bias. Comparison with the analytical effectiveness-NTU solution gave duty deviations of 0.4% to 0.6%; for the shell & tube configuration, the 1D counter-flow representation transfers 7.6% more heat than the one-shell-pass, two-tube-pass solution at the same NTU ($F_t = 0.845$), which quantifies the multi-pass effect omitted by the equivalent 1D model. The lumped wall holds for the plate configuration ($Bi \approx 0.03$) but not for the other two ($Bi = 1.29$ and 0.62). Under a 10 °C step decrease in the hot inlet temperature, SIMC-tuned PI control and feedforward plus PI control both return the outlet to within ± 0.5 °C of the setpoint in 3.5 s to 38 s, with ISE reductions of two to three orders of magnitude. In the cases studied, the static feedforward term was beneficial where the time constant exceeds the transport delay by a factor of three to four (double-pipe and shell & tube: recovery three to six times faster, ISE four to twenty-five times lower than with feedback alone), but not for the delay-dominated plate exchanger, because it acts before the disturbance reaches the outlet.

Several limitations are acknowledged. The shell & tube exchanger is an equivalent 1D counter-flow model, so applicability to controller design for real multi-pass units with non-uniform shell-side flow remains limited, and its scenario operates at a high cross-flow velocity and pressure drop. The radially lumped wall is not justified for two geometries; the steady-state balance is unaffected, but the transient wall response and the recovery metrics carry a corresponding uncertainty. The first-order explicit scheme introduces numerical diffusion and a CFL-limited time step, and the plate scenario operates partly below the data range of its correlation. Finally, without experimental transient data or multi-dimensional simulations, the dynamic predictions, including the recovery times and the geometry-dependent effect of the feedforward term, remain model-internal findings.

Nomenclature

Symbol	Description	Unit
$A_h, A_c, A_w; A_{\text{eff}}$	Flow areas (hot, cold); wall section; heat transfer area	m^2
$b, W, t_w; B, P_t, N_t$	Plate gap, width, thickness; baffle spacing, tube pitch, tube count	m; m, m, –
Bi	Biot number, $h_{\text{avg}} L_{\text{char}}/k_w$	–
$C_h, C_c, C_{\min}, C_r; C_{\text{sys}}$	Capacity rates, minimum, ratio; thermal capacitance	W/K, –; J/K
$c_p; c_v(x)$	Specific heat; initial profile function, Equation 6	J/(kg K); –
$D_{ti}, D_{to}, D_{si}; D_h, D_e$	Tube inner, tube outer, shell diameters; hydraulic, equivalent diameters	m
e	Control error, $T_{h,\text{out}} - T_{\text{sp}}$	°C
$f, f_d, f_{d0}, f_{d1}; f_1, f_2, f_3, f_{\text{ext}}$	Darcy friction factors; grid solutions (fine, medium, coarse)	–; °C
$F_s, F_t; GCI$	GCI safety factor; LMTD correction factor; Grid Convergence Index	–; %
h_h, h_c, h_{avg}	Convective coefficients (hot, cold, average)	W/(m^2 K)
ISE	Integral of squared error after t_{dist}	$°C^2$ s
k, k_w	Conductivity (fluid, wall)	W/(m K)
$K_p; K_c, \tau_I$	Process gain; PI gain and integral time	°C/(kg/s); (kg/s)/°C, s
L, L_{char}	Flow length; wall thickness	m
$\dot{m}_h, \dot{m}_c; \dot{m}_{c,\min}, \dot{m}_{c,\max}, \dot{m}_{c,\text{FF}}$	Mass flow rates; actuator limits; feedforward demand	kg/s
$N, N_{\text{ch}}; NTU, Nu, Pr, Re$	Nodes, channels per side; transfer units, Nusselt, Prandtl, Reynolds numbers	–
p, r	Observed order; refinement ratio	–
P_h, P_c	Wetted perimeters	m

Symbol	Description	Unit
$q_{h,w}, q_{w,c}; Q$	Heat flow per unit length (hot to wall, wall to cold); heat rate	W/m; W
R_w	Wall resistance per unit length	m K/W
$t, t_{\mathrm{dist}}, t_{\mathrm{end}}, t_{\mathrm{gi}}, t_r$	Time; disturbance onset; end; grid-study duration; recovery time	s
$T_h, T_w, T_c; T_{\mathrm{in}}, T_{\mathrm{out}}, T_{\mathrm{sp}}$	Hot, wall, cold temperatures; inlet, outlet, setpoint	°C
$u_h, u_c; U$	Velocities; overall heat transfer coefficient	m/s; W/(m^2 K)
$w_1, w_2; x$	Blending weights, Equation 17; axial coordinate	–; m
$\alpha_w; \beta, \phi$	Wall thermal diffusivity; chevron angle, enlargement factor	m^2/s; °, –
$\Delta P; \Delta t, \Delta x$	Pressure drop; time and spatial steps	kPa; s, m
$\varepsilon; \theta, \tau, \tau_c$	Effectiveness; dead time, time constant, SIMC closed-loop time constant	–; s
$\mu, \mu_w; \rho$	Viscosity (bulk, wall); density	Pa s; kg/m^3

References

[1] K. J. Åström and T. Hägglund, *Advanced PID Control*. John Wiley & Sons, Inc., 2006.

[2] G. Bylund, *Dairy Processing Handbook*. Tetra Pak Processing Systems AB, 1995.

[3] Y. A. Çengel and A. J. Ghajar, *Heat and Mass Transfer: Fundamentals and Applications*. McGraw Hill Education, 5th ed., 2015.

[4] V. Gnielinski, "New equations for heat and mass transfer in turbulent pipe and channel flow," *Int. Chem. Eng.*, vol. 16, no. 2, pp. 359–368, 1976.

[5] D. Q. Kern, *Process Heat Transfer*. McGraw-Hill, 1950.

[6] H. Martin, "A theoretical approach to predict the performance of chevron-type plate heat exchangers," *Chemical Engineering and Processing: Process Intensification*, vol. 35, no. 4, pp. 301–310, 1996.

[7] T. Zhao *et al.*, "A frequency domain dynamic simulation method for heat exchangers and thermal systems," *Energy*, vol. 286, p. 129552, 2024.

[8] M. Granda, M. Trojan, J. Taler, and D. Taler, "Transient modelling of heat exchangers using a steady-state model for low heat capacity media," *Energy*, vol. 327, p. 136466, 2025.

[9] R. Yang, C. T. Tran, and A. Zoughaib, "An analytical model to study the dynamic response of heat exchanger network," *Int. J. Heat Mass Transf.*, vol. 176, p. 121461, 2021.

[10] S. Mechhoud and Z. Belkhatir, "Adaptive bounded bilinear control of a parallel-flow heat exchanger," *Int. J. Adapt. Control Signal Process.*, vol. 39, pp. 320–331, Feb. 2025.

[11] J. Zou, T. Hirokawa, J. An, L. Huang, and J. Camm, "Recent advances in the applications of machine learning methods for heat exchanger modeling—a review," *Front. Energy Res.*, vol. 11, 2023. Art. no. 1294531.

[12] H. Togun *et al.*, "Machine learning in heat exchanger modeling: Recent trends and innovations," *International Communications in Heat and Mass Transfer*, vol. 169, p. 109920, 2025.

[13] S. B. Padmanabhan, M. T. Mabrouk, and B. Lacarrière, "Neural-accelerated dynamic modeling of heat pumps," *Appl. Therm. Eng.*, vol. 274, p. 126653, 2025.

[14] E. Diaz-Bejarano, F. Coletti, and S. Macchietto, "A model-based method for visualization, monitoring, and diagnosis of fouling in heat exchangers," *Ind. Eng. Chem. Res.*, vol. 59, pp. 4602–4619, Feb. 2020.

[15] S. Brooks, A. Yasin, K. Alatishe, and R. Roy, "Design and implementation of a self-cleaning heat exchanger using a digital twin," *SSRN Electronic Journal*, 2021.

[16] K. Shaikh *et al.*, "A review of recent advancements in the crystallization fouling of heat exchangers," *J. Therm. Anal. Calorim.*, vol. 148, no. 22, pp. 12369–12392, 2023.

[17] B. Sudarmanta, R. M. Wijayanto, G. Nugroho, A. Syaifudin, A. Setiyawan, and J. B. Ariateja, "Numerical study effect of fluidizing air to erosion pattern in circulating fluidized bed boiler," *The International Journal of Mechanical Engineering and Sciences*, vol. 1, pp. 17–26, July 2025.

[18] A. H. S. Putranto, V. S. Djanali, and B. A. Dwiyantoro, "Numerical study of savonius wind turbine rotor with elliptic angle shape variation," *The International Journal of Mechanical Engineering and Sciences*, vol. 3, pp. 44–53, July 2025.

[19] H. Novianto and P. Prabowo, "Numerical study of temperature and air velocity distribution in oil filling factory," *The International Journal of Mechanical Engineering and Sciences*, vol. 1, pp. 1–8, July 2025.

[20] L. F. Richardson, "IX. the approximate arithmetical solution by finite differences of physical problems involving differential equations, with an application to the stresses in a masonry dam," *Philosophical Transactions of the Royal Society of London, Series A: Containing Papers of a Mathematical or Physical Character*, vol. 210, pp. 307–357, Jan. 1911.

[21] I. B. Celik, U. Ghia, P. J. Roache, C. J. Freitas, H. Coleman, and P. E. Raad, "Procedure for estimation and reporting of uncertainty due to discretization in CFD applications," *J. Fluids Eng.*, vol. 130, July 2008.

[22] S. Skogestad, "Simple analytic rules for model reduction and PID controller tuning," *J. Process Control*, vol. 13, no. 4, pp. 291–309, 2003.

[23] J. P. Holman, *Heat Transfer*. McGraw Hill Higher Education, 10th ed., 2010.

[24] T. L. Bergman and F. P. Incropera, *Fundamentals of Heat and Mass Transfer*. Wiley Custom Learning Solutions, 7th ed., 2011.

[25] H. Martin, "N6 pressure drop and heat transfer in plate heat exchangers," in *VDI Heat Atlas*, pp. 1515–1522, Berlin, Heidelberg: Springer Berlin Heidelberg, 2010.

[26] S. V. Patankar, *Numerical Heat Transfer and Fluid Flow*. CRC Press, 2018.

[27] A. Muley and R. M. Manglik, "Experimental study of turbulent flow heat transfer and pressure drop in a plate heat exchanger with chevron plates," *J. Heat Transfer*, vol. 121, pp. 110–117, Feb. 1999.

[28] W. M. Kays and A. L. London, *Compact Heat Exchangers*. New York, NY, USA: McGraw-Hill, 1984.

[29] R. A. Bowman, A. C. Mueller, and W. M. Nagle, "Mean temperature difference in design," *Transactions of the American Society of Mechanical Engineers*, vol. 62, no. 4, pp. 283–293, 1940.